Flexible magnetic composites for light-controlled actuation and interfaces

Meng Li[a,b,1], Yu Wang[a,b,1], Aiping Chen[c], Arin Naidu[a,b], Bradley S. Napier[a,b], Wenyi Li[a,b], Carlos Lopez Rodriguez[b], Scott A. Crooker[d], and Fiorenzo G. Omenetto[a,b,e,f,2]

[a]Silklab, Tufts University, Medford, MA 02155; [b]Department of Biomedical Engineering, Tufts University, Medford, MA 02155; [c]Center for Integrated Nanotechnologies, Los Alamos National Laboratory, Los Alamos, NM 87545; [d]National High Magnetic Field Laboratory, Los Alamos National Laboratory, Los Alamos, NM 87545; [e]Department of Electrical and Computer Engineering, Tufts University, Medford, MA 02155; and [f]Department of Physics, Tufts University, Medford, MA 02155

Edited by David A. Weitz, Harvard University, Cambridge, MA, and approved June 26, 2018 (received for review April 4, 2018)

The interaction between light and matter has been long explored, leading to insights based on the modulation and control of electrons and/or photons within a material. An opportunity exists in optomechanics, where the conversion of radiation into material strain and actuation is currently induced at the molecular level in liquid crystal systems, or at the microelectromechanical systems (MEMS) device scale, producing limited potential strain energy (or force) in light-driven systems. We present here flexible material composites that, when illuminated, are capable of macroscale motion, through the interplay of optically absorptive elements and low Curie temperature magnetic materials. These composites can be formed into films, sponges, monoliths, and hydrogels, and can be actuated with light at desired locations. Light-actuated elastomeric composites for gripping and releasing, heliotactic motion, light-driven propulsion, and rotation are demonstrated as examples of the versatility of this approach.

soft robotics | optomechanics | light actuation | silk | elastomers

Actuators are components used to move a mechanical system or perform shape morphing, in response to certain stimuli. Among various mechanisms to induce mechanical deformation, light has distinguishing advantages of wireless control, and the capability of high-resolution and localized stimulation. Current photomechanical systems are mainly based on liquid crystal (1–4), optical gradient force (5), shape memory polymers (6, 7), or inequivalent expansion of gradient materials (8–10). The actuating direction mostly depends on incident light direction or material gradient direction. Most optomechanical devices can perform simple movement such as bending (3, 6, 10, 11), twisting (4, 12), or expansion (1, 13) with simple light modulation, and achieve complex movement like folding (14, 15), walking (8, 16), swimming (17, 18), or waving (2) only with complex light patterning or structured design. There are many occasions, however, where these modulations cannot be satisfied, and the versatility is limited by the specific design.

Ferro-/ferrimagnetic materials, which are widely employed for magnetic actuators (19, 20), become paramagnetic above their Curie temperature, losing their spontaneous magnetization. However, most magnetic materials used in magnetic actuators have high Curie temperature: 857 K for magnetite Fe_3O_4 (21), 1,043 K for iron, 1,394 K for cobalt and 631 K for nickel (22), making it difficult to significantly change their magnetic properties at room temperature. Temperature-sensitive ferrites have been used for actuators (23, 24) and microrobots (25) based on their temperature-dependent variation of magnetic properties. They are alloys made mainly of iron and nickel, which can have Curie temperature as low as 310 K. However, they are constrained by brittle and bulky material formats lacking the mechanical flexibility that is generally required for use in actuation and soft robotics. Chromium dioxide (CrO_2) is a ferromagnetic material that was once widely used in manufacturing data storage devices in the midlate 20th century (26). Pure and unmodified CrO_2 has a considerably lower Curie temperature of 391 K (27), allowing the opportunity to achieve large changes in magnetization with relatively small changes in temperature over a convenient temperature range.

We introduce here light-responsive magnetic composites by incorporating CrO_2 in multiple flexible, elastomeric, and mechanically robust, durable materials. Optically induced demagnetization provides multiple opportunities for wireless actuation, shape morphing, and deformation in response to light in easy-to-use formats. Because of their polymorphic nature along with their flexibility and high failure strain, biopolymers and elastomers are used as magnetically inert host material matrices for ferromagnetic dopants. The former trait allows diverse end-material formats, adjustable mechanical properties, and programmable functions through directed assembly while the latter allows for longer actuator lifetime and good reproducibility. Specifically, silk fibroin (SF) and polydimethylsiloxane (PDMS) are used as the base materials to generate the optomechanical composites. SF is a versatile biocompatible, polymorphic, and biodegradable biopolymer (28) with excellent optical properties (29–31) that has been extensively explored for technological and biomedical applications (32, 33), while PDMS is a widely used transparent elastomer used in fields such as micromechanics, prototyping, analytical chemistry, among others (34–36). The composites are fabricated by direct incorporation of ferromagnetic CrO_2 powder within the biopolymeric and elastomeric matrices precursors during material formation. The ferromagnetic powder has an average particle size on the order of 10 μm, and is pretreated with sodium bisulfite to generate a reduced barrier surface layer, using methods described in literature (37).

Significance

This approach offers a platform for controlled, light-induced motion with easily accessible equipment and facile manufacturing processes. Utility can be envisioned for flexible, simple, and cost-effective actuators from the micro- to the macroscale. Additional opportunity is offered by the ability of these composites to perform heliotactic motion, enabling formats that respond and track light sources such as the sun.

Author contributions: M.L. and F.G.O. designed research; M.L., Y.W., A.C., A.N., B.S.N., W.L., C.L.R., and S.A.C. performed research; M.L. contributed new reagents/analytic tools; M.L., Y.W., A.C., A.N., B.S.N., W.L., C.L.R., S.A.C., and F.G.O. analyzed data; and M.L., A.C., S.A.C., and F.G.O. wrote the paper.

The authors declare no conflict of interest.

This article is a PNAS Direct Submission.

[1]M.L. and Y.W. contributed equally to this work.

[2]To whom correspondence should be addressed. Email: fiorenzo.omenetto@tufts.edu.

This article contains supporting information online at www.pnas.org/lookup/suppl/doi:10.1073/pnas.1805832115/-/DCSupplemental.

Published online July 23, 2018.

The treatment prevents oxidation reactions with water and organic solvents, allowing for the CrO_2 powder to be directly mixed with SF or PDMS without introducing any visible aggregation. The different material forms of SF and elastomers/CrO_2 composites will be hereafter referred to as "magnetic" for clarity. The mass ratio of CrO_2 to SF or PDMS base reagent will be denoted by the percentage (for example, a film with 50 wt % CrO_2 relative to SF will be referred to as 50% magnetic SF film). Unless otherwise noted, all magnetic PDMS indicates a 50% CrO_2 mass ratio.

To illustrate the facile preparation of such light-responsive composites and the multiple possible forms obtainable, several material formats were generated, ranging from magnetic films, both rigid and elastic, to sponges, monoliths, and hydrogels (Fig. 1). It is worth observing that the freestanding magnetic SF film is flexible and not transparent (Fig. 1*A*), and that the addition of CrO_2 into the SF matrix causes physical cross-linking of the protein, inducing β-sheet structure (*SI Appendix*, Fig. S1), thereby rendering the film (largely) water insoluble. Additionally, the mechanical properties of the magnetic SF composite film are modified with an increase in Young's modulus in comparison with pure SF films (*SI Appendix*, Fig. S2).

The CrO_2 particles are uniformly distributed in plane (*SI Appendix*, Fig. S3), but a gradient structure is present out of plane (Fig. 1*B*). The composite side with higher CrO_2 concentration will be referred to subsequently as the C side, while the other will be either the S side (for SF composites) or the P side (for PDMS composites). This gradient is generated as part of the drying process when particle sedimentation leads to a higher CrO_2 concentration on one side (the bottom) of the film. The CrO_2 gradient can be seen in SEM images of the films' cross-section (Fig. 1 *C* and *F*). Magnetic PDMS can be easily molded into different shapes and can be formed into various patterns (Fig. 1 *D* and *E*). Additional light-active magnetic material formats can be obtained by leveraging SF's polymorphism to generate magnetic sponges, monoliths, and hydrogels (Fig. 1 *G*–*I*). These composites show strong magnetic responses, and can be simply manipulated with a permanent magnet (Fig. 1*J*).

The materials as composed are light-responsive and can be actuated following the simple mechanism outlined in Fig. 1*K*. A CrO_2 composite cantilever is formed and placed in a magnetic field generated by either a permanent magnet or an electromagnet. The field amplitude exceeds the material's coercivity and thus, the magnetic force is attractive. The cantilever bends toward the magnet and reaches an equilibrium state where the

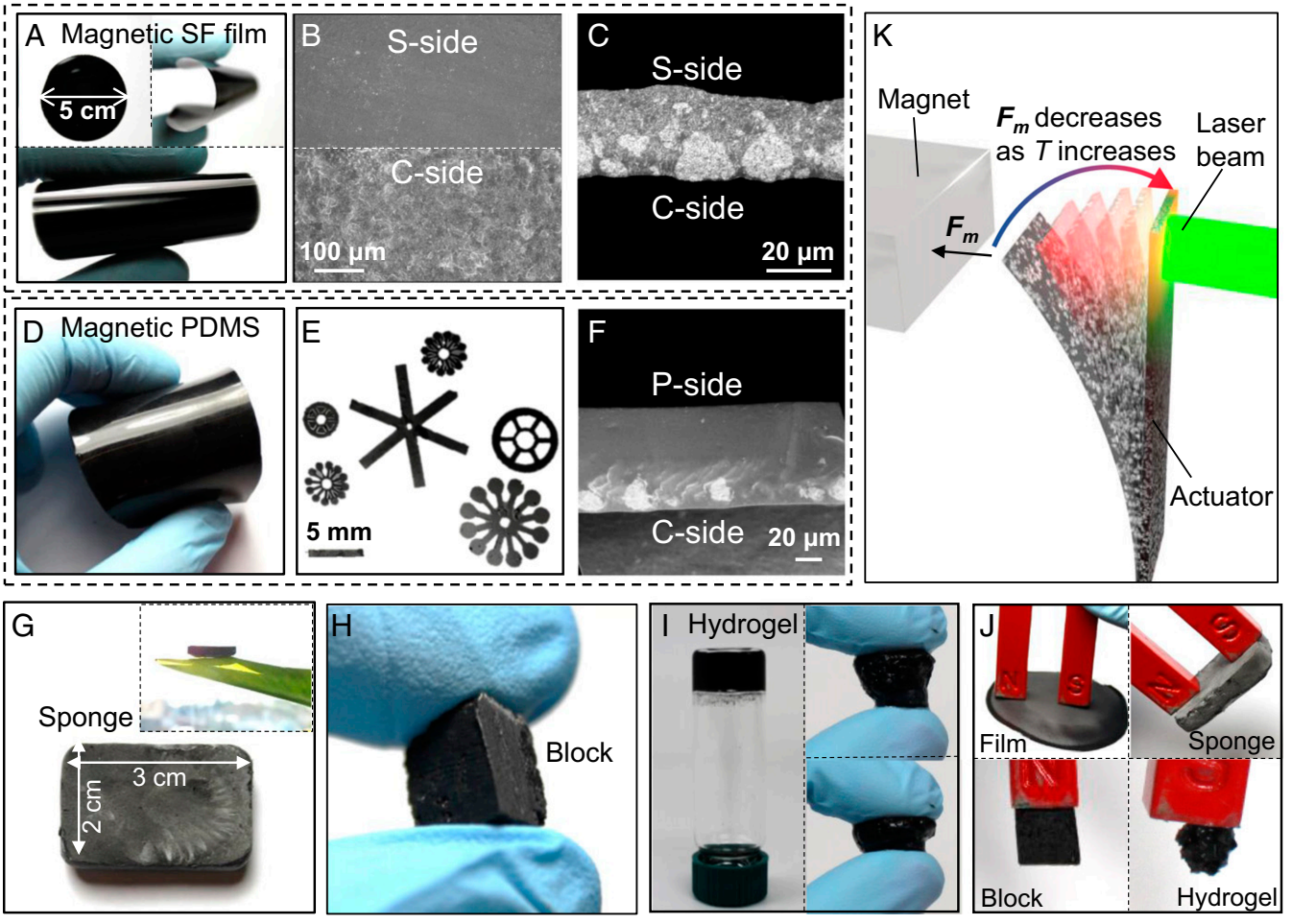

Fig. 1. Multiple magnetic composite formats and light-actuation mechanism. (*A*–*C*) Photos and SEM images of a 50% magnetic SF film. (*A*) Photos from top and side view of a bending film. (*B*) SEM images of the S-side (*Top*) and the C-side (*Bottom*) surfaces. (*C*) SEM images of the cross-section. (*D*–*F*) Photos and SEM images of magnetic PDMS sheet. (*D*) A flexible 20% magnetic PDMS slab with 1.5-mm thickness. (*E*) Different patterns that are laser-cut from magnetic PDMS membrane of 100-μm thickness. (*F*) SEM image of the cross-section of a magnetic PDMS sheet. (*G*) A 50% magnetic SF sponge. (*Inset*) Photo shows the light-mass sponge placed on top of a plant leaf. (*H*) A 20% magnetic SF block by sol-gel transformation. (*I*) A 50% magnetic SF hydrogel made in a glass vial; another piece is pressed by fingers. (*J*) Direct manipulation of different composite forms with a permanent magnet. (*K*) Schematic of the actuation of a composite cantilever by photothermal demagnetization.

magnetic force and elastic force are balanced. When the magnetic composite is illuminated by light, such as a laser or sunlight, it converts photonic energy into thermal energy, causing an increase of the cantilever temperature. Because of the ferromagnetic nature of the material, as the temperature T goes up, the local magnetic susceptibility χ is decreased. The magnetic attractive force applied on the sample is $\boldsymbol{F} = (\boldsymbol{m} \cdot \nabla)\boldsymbol{B}$, with the magnetization $\boldsymbol{m} = (\chi/\mu_o)\boldsymbol{B}$. While the magnetic field profile stays unchanged, the force $\boldsymbol{F}$ decreases with lower susceptibility χ resulting from higher temperature. According to the Euler–Bernoulli beam theory (38), a smaller magnetic force leads to a smaller beam deflection, because of the decreasing load. When the light source is removed, the actuator temperature equilibrates to the surrounding temperature, causing the magnetization to increase with the temperature decrease, thereby reversing the deflection.

Material response time and performance depend on the photothermal conversion efficiency, since the temperature change induced by the light directly determines the amplitude and the time scale of magnetization loss. The effect is analyzed by forming magnetic SF film strips (8 mm× 2 mm) with different CrO_2 loading percentages, and evaluating the material response when exposed to a 2-cm-diameter continuous-wave laser beam ($\lambda = 532$ nm). Film thickness for different loading percentages is listed in *SI Appendix*, Table S1. The light-intensity distribution on a transverse plane of the beam-propagation path has a Gaussian profile, and the sample is located in the center of the beam. The total power incident on the sample is calculated by integrating the Gaussian intensity distribution of light with respect to the sample location and its surface area. The temperature is measured with an IR camera by averaging over a 1-min period after the temperature stabilizes. The temperature variation is found to be linearly dependent on the incident power at specific loading percentages (Fig. 2*A*). A 100% magnetic SF film exhibits a temperature increase of 105 K from room temperature (T_{room} = 303 K) for an incident power P = 145 mW. The maximum temperatures are not significantly affected by different CrO_2 loading percentages, and are found to be within 12 K of one another (Fig. 2*A*, *Inset*). This is attributed to the high light absorption at all loading percentages (*SI Appendix*, Fig. S4). The thermal relaxation time τ is measured by sequential exposure to light (on/off laser switching cycles), and estimated with an exponential function according to Newton's law of cooling (39):

$$\text{heating}: T = T_{\max} - (T_{\max} - T_{room})e^{-(t/\tau)},$$

$$\text{cooling}: T = T_{room} - (T_{room} - T_{\max})e^{-(t/\tau)},$$

where T_{max} and T_{room} are the temperature from heating and room temperature, respectively. The thermal relaxation time τ

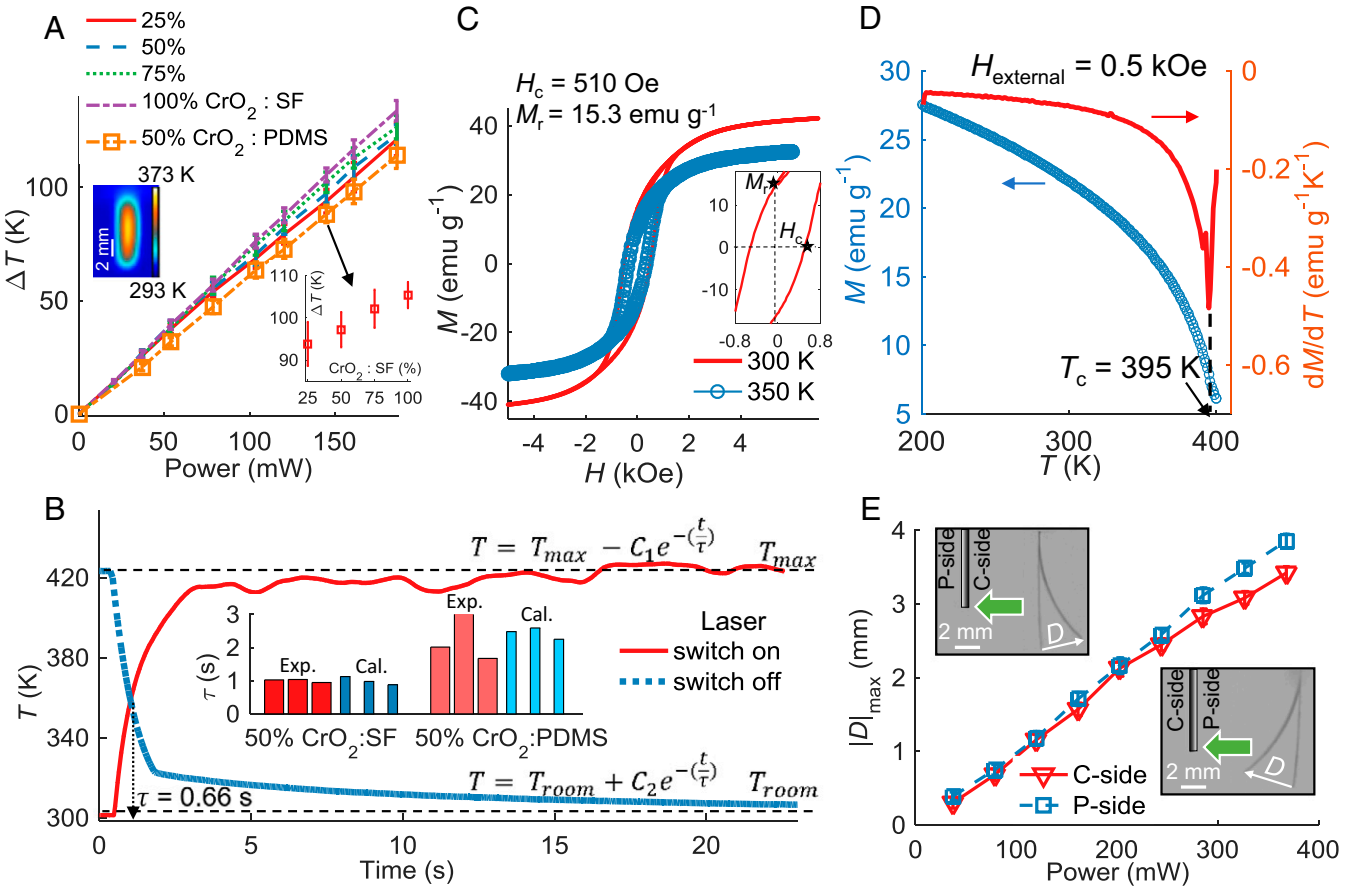

Fig. 2. Photothermal responses and thermal-demagnetization properties. (*A*) Average stabilized temperature rise of magnetic SF film strips (2 mm × 8 mm) with different loading percentages (25, 50, 75 and, 100%) and 50% magnetic PDMS strip under different laser powers. The thermal camera image is for 50% magnetic PDMS sample under 120-mW illumination. (*Inset*) Graph shows the temperature rise at different loading percentages of magnetic SF film under 145-mW laser power. (*B*) Heating and cooling curve of a 50% magnetic SF film strip under 186-mW laser illumination. (*Inset*) Bar graph is experimental (thick bars) and calculated (thin bars) τ values for three 50% magnetic SF and three 50% magnetic PDMS strips with laser power 37 mW. (*C*) Hysteretic magnetization of pretreated CrO_2 powder at 300 and 350 K. (*Inset*) Curve at 300 K around zero magnetic field. (*D*) Magnetization of pretreated CrO_2 powder in the temperature range from 200 to 400 K (blue) and the first derivative of $M(T)$ (red). (*E*) The maximum displacement of the tip of a 50% magnetic PDMS strip (2 mm × 8 mm × 0.1 mm) for laser illumination on both C and P sides.

for a 24-μm-thin 50% magnetic SF film is 0.66 ± 0.04 s (mean ± 95% CI) under illuminating power 190 mW (Fig. 2*B*). For a 110-μm-thick magnetic PDMS, with same illumination power, τ value is found to be 1.92 ± 0.04 s (*SI Appendix*, Fig. S5). τ can also be theoretically estimated by $\tau = \rho Cb/h$ (9), where ρ is the sample density, C is the heat capacity, b is the sample thickness, and h is the heat convection coefficient. Using the measured value of C, the calculated τ values are in good accordance with experimental values (Fig. 2*B*, *Inset*), suggesting that CrO_2 dominates the heating process. This is further corroborated by the fact that illumination occurs from the C side, and the thermal camera mainly measures the surface temperature (*SI Appendix*, *Supplemental Text* and Table S2). Thermal efficiency is calculated by fitting the cooling curve of all of the samples. The efficiency of converting photonic energy to thermal energy is beyond 55% for all of the loading percentages of magnetic SF composite and for 50% magnetic PDMS (*SI Appendix*, *Supplemental Text* and Fig. S6). Exposure of the magnetic composite materials to the temperatures above does not significantly affect the material or cause it to undergo weight loss, as confirmed by thermogravimetric analysis of the samples which shows a thermal degradation onset temperature 550 and 631 K for 50% magnetic SF and 50% magnetic PDMS, respectively (*SI Appendix*, Fig. S7).

The effect of the pretreatment process on the magnetic properties of the CrO_2 powder is also investigated. Magnetic hysteresis loops are measured for pretreated CrO_2 powder at 300 and 350 K (Fig. 2*C*), showing high saturated magnetization values of 43.2 and 35 emu g^{-1}, respectively. The received nontreated CrO_2 has saturated magnetization of 80.8 emu g^{-1} (*SI Appendix*, Fig. S8), revealing a trade-off between the stability necessary for material processing and a variation in the baseline magnetic responses. The measured remnant magnetization M_r and coercivity H_c is 15.3 emu g^{-1} and 510 Oe, consistent with values reported in the literature (24, 40). The Curie temperature, T_c, is defined as the point where the first derivative dM/dT has largest magnitude (41), and is measured to be 395 K (Fig. 2*D*). The discrepancy from tabulated values is attributed to the introduction of the pretreatment barrier/protective layer that may lead to an increase of the Curie temperature compared with pure, unmodified CrO_2 (42).

The vertical CrO_2 gradient described previously causes an inequivalent expansion of the two sides of the magnetic composite when exposed to heat (*SI Appendix*, Fig. S9), humidity (*SI Appendix*, Fig. S10), and light, resulting in mechanical deformation. To quantify light-driven actuation, a simple elastomeric cantilever (100 μm thick, 8 mm × 2 mm) is evaluated under different illuminating power as shown in Fig. 2*E*. The cantilever displacement D is defined as the displacement of the cantilever tip compared with the original position with no illumination. The sign of the displacement D is defined as negative when the side facing the incident light expands (to the left of the image), while defined as positive when the back side of the incident light expands (to the right side of the image). For received laser power of 368 mW, D reaches −3.86 ± 0.10 mm for P side and 3.42 ± 0.09 mm for C-side illumination.

Fig. 3*A* shows frames of recorded videos at t = 0, 2.5, 5, 7.5 s after laser is switched on and 10 s after laser is switched off. Values of the measured deflection D plotted against time for different laser intensities are shown in Fig. 3*B*. When the cantilever is lifted by the electromagnet, the magnetic field is 30 mT at the cantilever tip. With higher laser power, the actuating speed is faster and the corresponding maximum displacement is larger. As one can see in Fig. 3*B*, for higher laser powers, the cantilever does not recover to its original position after the laser is switched off. With repeated heating and cooling, the cantilever always returns to the same position (within 100 μm). This can be explained as follows: before each experiment, the cantilever is magnetized horizontally with an ∼400-mT external field to maximize the magnetic force between the cantilever and the electromagnet. The magnetic field from the electromagnet does not exceed the coercivity of the cantilever. When illuminated by the laser, the coercivity decreases as the temperature rises, decreasing the cantilever's net magnetization since the magnetic field is weaker as the distance is greater from the electromagnet. Thus, the total attractive force between the cantilever and the electromagnet is smaller after the heating process compared with the initial condition, which results in a smaller deflection of the cantilever after the light is switched off. By directing light on different sides (C or P side) of the composites, significantly different actuations can be achieved (Fig. 3*B*, *Inset*) for the same incident light power. When illuminated on the C side with 160 mW, after reaching the original vertical alignment (D = 4.46 mm), the displacement continues to increase to 5.38 ± 0.11 mm because of the thermal expansion. Finally, the elastomeric composite was evaluated for performance, cycling the cantilever 300 times by switching the laser on/off with 5 s/5 s period. The performance did not deteriorate, which implies a mechanical operation in the elastic range and a total recovery of the magnetization when the temperature decreases (Fig. 3*C*).

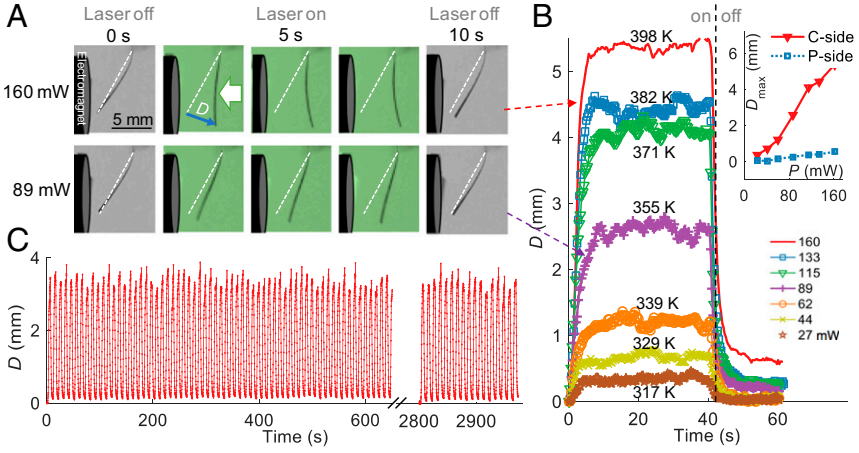

Fig. 3. Light-induced actuation of a 50% magnetic PDMS strip. (*A*) Actuation process under 89-mW/160-mW laser illumination and 30-mT external magnetic field. The white arrow indicates the light incident on the C side of the strip. (*B*) Sample tip displacement as a function of time under different laser power with C-side illumination. The maximum temperature is marked for each curve. (*Inset*) Maximum measured displacement for both C- and P-side illumination. (*C*) Cyclic response when the strip is illuminated by 100-mW laser power at 50% cycle with a period of 10 s for ∼300 cycles.

These types of composite material strategies and their interplay with light can be used to achieve complex multiscale untethered actuation, and could generate interesting applications for reconfigurable surfaces, locomotion, or soft robotics. Demonstrator devices based on this approach were fabricated to illustrate complex movement with simple illumination. The ability to generate an optomagnetic elastomeric composite can enable soft grippers to capture and release objects in response to light.

The device is shown in Fig. 4*A*. A shaped CrO_2/PDMS "claw-like" structure with multiple "fingers" is attached to the tip of an optical fiber (which only serves as a mechanical support). This structure can be used as a small gripper tool, given that the fingers of the claws experience cyclical tightening and loosening in response to the light-induced demagnetization and the changing magnetic force. A demonstration of this functionality has been carried out by having the structure grab and move an object (of size 4 mm × 4 mm × 3.5 mm and mass m = 2 mg) placed in proximity to the magnet. The light used to actuate the device is provided by a laser (λ = 532 nm, P_{total} = 3 W, beam diameter w ~ 1 cm) that illuminates the structure from above and demagnetizes the "claw." When the laser is switched on, the object is gripped, lifted, and eventually released away from its original location in a few ($t \sim 6$) seconds (Fig. 4*B* and Movie S1). It is expected that larger loads can be handled with different combination of materials and actuating magnets.

The same structure can also act like a resonator by suspending the structure above a permanent magnet, so that the construct is pulled and bent toward the magnet and the fingers are closed. As the heat accumulates in the structure and temperature gradually increases, the attractive force on the structure correspondingly decreases, leading to the unbending of the optical fiber and opening of the fingers. While still being in the proximity of the magnetic field, the light-responsive structure is attracted toward the magnet and the optical fiber bends again and the fingers close. The resonating cycle continues as long as the light is kept on (Movie S2).

Compared with magnetic actuators, the use of light-responsive materials offers the advantage of being able to localize the control and selectively actuate portions of the material. This can be shown by reshaping a piece of 130-μm-thick magnetic PDMS film with 20 wt % CrO_2 into a flower-like geometry with six "petals" of equal dimensions (4 mm × 1 mm). Because of the magnetic force between the permanent magnet and the film, the petals are lifted toward the magnet located above as shown in Fig. 4*C*. Directing light onto an individual petal allows it to be moved without affecting the others. By mounting the structure onto a post, it is possible to address the petals sequentially by rotating the post in the path of the laser beam, causing that portion to heat up, lose its partial magnetization, and "open" under gravity. In this way, the six petals can be alternatively and independently actuated (Movie S3). These composites can be rationally designed to move with (heliotropic) or against (contraheliotropic) the direction of incident light, which is usually not the case for uniform liquid crystal based photoactuators. It is worth noting that in this case, the actuation does not depend on the CrO_2 gradient and the sample can be placed with either side facing up, unlike other photothermal actuators with gradient structures. These types of composites can also respond to solar irradiance. As an example, sunlight was used to control the vertical position of a levitated permanent magnet (*SI Appendix*, Fig. S11). A magnetic sponge composite is placed above a levitated magnet floating between two sheets of pyrolytic graphite. Focusing sunlight onto the sponge changes its magnetization and displaces the permanent magnet vertically. The magnet can be also moved in plane by focusing sunlight on different spots of the magnetic SF sponge.

As a final demonstration, a Curie engine powered by light (Fig. 4*D*) was realized by reshaping a 1.5-mm-thick magnetic PDMS slab into a ring structure that can freely rotate on a stainless-steel needle post in the presence of a permanent

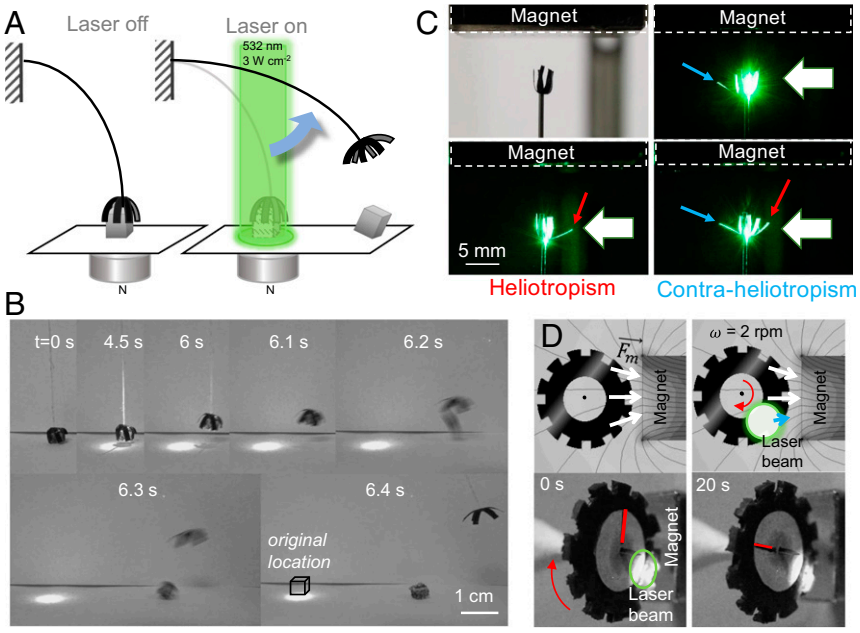

Fig. 4. Demonstrators of optomechanical actuators. (*A*) Schematic illustrating the operation of a magnetic composite gripper. (*B*) Sequential images of the lifting and release of a small cube. (*C*) A "flower"-shaped magnetic PDMS sheet locally actuated by light with the illustration of heliotropism (red arrow) and contraheliotropism (blue arrow). The white arrow indicates the incident light direction. The dashed line outlines the edge of the permanent magnet. (*D*) Schematic and images of a Curie engine (outer diameter 3 cm) rotating with fixed laser illumination (green circle) and a permanent magnet (5 cm × 2.5 cm × 1 cm). The white and blue arrows in the schematic diagram indicate the magnetic force direction and its relative amplitude on the rotor.

magnet. The laser beam (λ = 532 nm, P_{total} = 1.8 W, beam diameter ~ 1 cm) is focused onto a fixed spot on the ring and neither the magnet nor the laser beam are moved. Local demagnetization at the illuminated spot leads to local decrease of the magnetic susceptibility, while the magnetic susceptibility of the rest of the rotor stays unchanged. This results in an unbalanced net force in vertical direction which starts the rotation. The Curie engine as constructed can continuously rotate at a speed of 2 rpm (Movie S4).

The concepts presented here represent different instances of a composite platform that merges optomechanical and magnetic functions. Multiple material formats, manufacturing approaches, characterization, and initial device demonstration for light-activated material systems and actuators provide the underpinnings for expanded opportunities in functional, flexible materials. Additional utility will be added by magnetic field control, and patterned material designs with opportunities in non-homogeneous shape morphing, such as origami folding or auxetic material forms, valves and switches in microfluidic devices, or sun tracking systems are among the possible options offered by the platforms. Tailored light control can offer further control through shaped wavefronts, diffractive optics, and multispectral operation which can be matched to specific resonant codopants such as plasmonic nanoparticles. Alternative device designs along these lines open promising directions for future actuator concepts, particularly when coupled with flexible electronic or soft-robotic platforms, and new modes of wireless, untethered dynamic interfaces.

ACKNOWLEDGMENTS. We thank the Cebe research group for their help with thermogravimetric analysis and differential scanning calorimetry measurements, and thank Prof. Xiaocheng Jiang and Prof. Iryna Zenyuk for the valuable discussion. The authors acknowledge support from Office of Naval Research Grant N00014-16-1-2437 for this work. Work at Los Alamos National Laboratory was performed at the Center for Integrated Nanotechnologies [an Office of Science User Facility operated for the US Department of Energy (DOE) Office of Science] and also at the National High Magnetic Field Laboratory, supported by National Science Foundation (NSF) Grant DMR-1157490, the State of Florida, and the US DOE. This work was performed in part at the Center for Nanoscale Systems (CNS), a member of the National Nanotechnology Coordinated Infrastructure Network (NNCI), which is supported by the NSF under NSF Award 1541959. CNS is part of Harvard University.

1. Lv J-A, et al. (2016) Photocontrol of fluid slugs in liquid crystal polymer microactuators. *Nature* 537:179–184.
2. Gelebart AH, Mulder DJ, Vantomme G, Schenning APHJ, Broer DJ (2017) Making waves in a photoactive polymer film. *Nature* 546:632–636.
3. Wani OM, Zeng H, Priimagi A (2017) A light-driven artificial flytrap. *Nat Commun* 8: 15546.
4. Iamsaard S, et al. (2014) Conversion of light into macroscopic helical motion. *Nat Chem* 6:229–235.
5. van Thourhout D, Roels J (2010) Optomechanical device actuation through the optical gradient force. *Nat Photonics* 4:211–217.
6. Leng J, Zhang D, Liu Y, Yu K, Lan X (2010) Study on the activation of styrene-based shape memory polymer by medium-infrared laser light. *Appl Phys Lett* 96:111905.
7. Yang H, et al. (2017) 3D printed photoresponsive devices based on shape memory composites. *Adv Mater* 29:1701627.
8. Mu J, et al. (2015) Origami-inspired active graphene-based paper for programmable instant self-folding walking devices. *Sci Adv* 1:e1500533.
9. Zhang X, et al. (2014) Photoactuators and motors based on carbon nanotubes with selective chirality distributions. *Nat Commun* 5:2983.
10. Tai Y, Lubineau G, Yang Z (2016) Light-activated rapid-response polyvinylidene-fluoride-based flexible films. *Adv Mater* 28:4665–4670.
11. Wang T, Torres D, Fernández FE, Wang C, Sepúlveda N (2017) Maximizing the performance of photothermal actuators by combining smart materials with supplementary advantages. *Sci Adv* 3:e1602697.
12. Wang M, Lin B-P, Yang H (2016) A plant tendril mimic soft actuator with phototunable bending and chiral twisting motion modes. *Nat Commun* 7:13981.
13. Lu X, Guo S, Tong X, Xia H, Zhao Y (2017) Tunable photocontrolled motions using stored strain energy in malleable azobenzene liquid crystalline polymer actuators. *Adv Mater* 29:1606467.
14. Liu Y, Shaw B, Dickey MD, Genzer J (2017) Sequential self-folding of polymer sheets. *Sci Adv* 3:e1602417.
15. Gelebart AH, Mulder DJ, Vantomme G, Schenning APHJ, Broer DJ (2017) A rewritable, reprogrammable, dual light-responsive polymer actuator. *Angew Chem Int Ed Engl* 56:13436–13439.
16. Wang L, et al. (2015) A bioinspired swimming and walking hydrogel driven by light-controlled local density. *Adv Sci (Weinh)* 2:1500084.
17. Dai B, et al. (2016) Programmable artificial phototactic microswimmer. *Nat Nanotechnol* 11: 1087–1092.
18. Palagi S, et al. (2016) Structured light enables biomimetic swimming and versatile locomotion of photoresponsive soft microrobots. *Nat Mater* 15:647–653.
19. Xu X, et al. (2015) Self-sensing, ultralight, and conductive 3D graphene/iron oxide aerogel elastomer deformable in a magnetic field. *ACS Nano* 9:3969–3977.
20. Fuhrer R, Schumacher CM, Zeltner M, Stark WJ (2013) Soft iron/silicon composite tubes for magnetic peristaltic pumping. Frequency-dependent pressure and volume flow. *Adv Funct Mater* 23:3845–3849.
21. Shpak AP, Gorbyk PP (2009) *Nanomaterials and Supramolecular Structures. Physics, Chemistry, and Applications* (Springer, Heidelberg).
22. Buschow KHJ, et al. (2001) *Encyclopedia of Materials: Science and Technology* (Elsevier, Amsterdam).
23. Mizutani Y, Ebisawa M, Otani Y, Umeda N (2008) Optically three-dimensional control of magnetic levitation using temperature-sensitive ferrite. *Jpn J Appl Phys* 47: 3461–3465.
24. Hashimoto E, Uenishi Y, Tanaka H, Watabe A (1995) Development of a thermally controlled magnetization actuator (TCMA) for a micromachined motor. *Electron Commun Jpn* 2:96–103.
25. Yoshizawa T, Hayashi D, Yamamoto M, Otani Y (2001) A walking machine driven by a light beam. *Proc SPIE* 4564:229–237.
26. Buxbaum G, Pfaff G, eds (2010) *Industrial Inorganic Pigments* (Wiley-VCH, Weinheim, Germany).
27. Chamberland BL (1977) The chemical and physical properties of CrO2 and tetravalent chromium oxide derivatives. *Crit Rev Solid State Mater Sci* 7:1–31.
28. Rockwood DN, et al. (2011) Materials fabrication from Bombyx mori silk fibroin. *Nat Protoc* 6:1612–1631.
29. Amsden JJ, et al. (2010) Rapid nanoimprinting of silk fibroin films for biophotonic applications. *Adv Mater* 22:1746–1749.
30. Toffanin S, et al. (2012) Low-threshold blue lasing from silk fibroin thin films. *Appl Phys Lett* 101:91110.
31. Xu L, et al. (2016) High-Q silk fibroin whispering gallery microresonator. *Opt Express* 24:20825–20830.
32. Tao H, Kaplan DL, Omenetto FG (2012) Silk materials–A road to sustainable high technology. *Adv Mater* 24:2824–2837.
33. Omenetto FG, Kaplan DL (2008) A new route for silk. *Nat Photonics* 2:641–643.
34. Vatankhah-Varnosfaderani M, et al. (2017) Mimicking biological stress-strain behaviour with synthetic elastomers. *Nature* 549:497–501.
35. Harsányi G (2000) Polymer films in sensor applications. A review of present uses and future possibilities. *Sens Rev* 20:98–105.
36. Seethapathy S, Górecki T (2012) Applications of polydimethylsiloxane in analytical chemistry: A review. *Anal Chim Acta* 750:48–62.
37. Bottjer WG, Ingersoll HG (1970) US Patent 3,512,930 (May 19, 1970). https://www.google.sr/patents/US3512930.
38. Bauchau OA, Craig JI, eds (2009) *Structural Analysis. With Applications to Aerospace Structures* (Springer, Dordrecht, The Netherlands).
39. Gockenbach M, Schmidtke K (2009) Newton's law of heating and the heat equation. *Involve* 2:419–437.
40. Onodera S, Kondo H, Kawana T (1996) Materials for magnetic-tape media. *MRS Bull* 21:35–41.
41. Fabian K, Shcherbakov VP, McEnroe SA (2013) Measuring the Curie temperature. *Geochem Geophys Geosyst* 14:947–961.
42. Coey JMD, Berkowitz AE, Balcells L, Putris FF, Barry A (1998) Magnetoresistance of chromium dioxide powder compacts. *Phys Rev Lett* 80:3815–3818.